



Photocatalytic Degradation of Methylene Blue by Using ZnO/Longan Seed Activated Carbon Under Visible-Light Region

Nguyen Van Hung¹ · Bui Thi Minh Nguyet² · Nguyen Huu Nghi¹ · Dinh Quang Khieu³

Received: 8 June 2020 / Accepted: 28 August 2020 / Published online: 5 September 2020
© Springer Science+Business Media, LLC, part of Springer Nature 2020

Abstract

In the present study, the synthesis of zinc oxide/longan seed activated carbon material (ZnO/LSAC) and its photocatalytic activity under the visible-light region are demonstrated. The pyrolysis of the carbonized material prepared from longan seeds and zinc acetate in the alkaline medium was conducted to manufacture ZnO/LSAC. The obtained material was characterized by using X-ray diffraction, Fourier transformation-infrared spectroscopy, high-resolution transmission electron microscopy, energy-dispersive X-ray elemental mapping observation, nitrogen adsorption/desorption isotherms, ultraviolet-diffuse reflectance spectroscopy (DRS–UV–Vis), and photoluminescence spectra. The ZnO nanoparticles with 20–30 nm in diameter are highly dispersed on the LSAC matrix. The combination of ZnO with LSAC promotes visible-light absorption. The photocatalytic activities of the prepared composite were evaluated for the degradation of methylene blue (MB) under visible-light irradiation. The kinetics and mechanism for photodegradation were addressed. The kinetic data and equilibrium data fit the modified Langmuir–Hinshelwood model. Introducing C to ZnO lattice creates an intermediate energy level and narrows the absorption energy, which results in the visible-light-driven photocatalytic activity of ZnO/LSAC. Reusability studies show that the catalyst retains its original activity even after the third cycle of reuse. Besides MB, the present catalyst could catalyze the photodegradation of other dyes, such as rhodamine B, congo red, and methyl orange.

Keywords Zinc oxide · Longan seed · Biomass carbon · Photodegradation · Methylene blue

1 Introduction

Various metal oxides and sulfides, such as TiO₂, SnO₂, ZnO, Bi₂MoO₆/Bi₂S₃, and MoS₂/CdS, have been used as photocatalysts for the degradation of toxic organic compounds and photocatalytic hydrogen evolution applications [1, 2]. Among the metal oxides, ZnO is a favorable semiconductor

material in the photodegradation of contaminants [3]. However, ZnO exhibits various disadvantages, such as highly photocorrosive nature and the fast recombination of the photo-induced electron–hole pairs [4–6]. Moreover, its photocatalytic activity is limited in the UV region of the spectrum due to its wide bandgap energy [5–9]. Therefore, to enhance the adsorption of visible light, ZnO is doped with transition metals (Cu, Fe, La, ...) and non-metals (S, N, and C) or supported on the substrates (activated carbon, alumina, silica, etc.) [10–13]. Among the support materials, activated carbon has been widely used to form ZnO/activated carbon composite due to its large surface area, high conductivity, and chemical stability. The formation of ZnO/activated carbon is believed to create energy sub-levels in the bandgap of the material by introducing C to the ZnO lattice and thereby decreasing its energy gaps. Besides, the prolonged existence of photogenerated electrons and holes is improved by the transfer of the photoexcited electrons to C on the surface of the catalyst [6]. Therefore, the ZnO modified with activated carbon possesses three advantages of redshift: reducing its

Electronic supplementary material The online version of this article (<https://doi.org/10.1007/s10904-020-01734-z>) contains supplementary material, which is available to authorized users.

✉ Nguyen Van Hung
nguyenvanhung@dthu.edu.vn

✉ Dinh Quang Khieu
dqkhieu@hueuni.edu.vn

¹ Center for Chemistry Analysis, Dong Thap University, Cao Lanh 81000, Vietnam

² Department of Organic Chemistry, Dong Thap University, Cao Lanh 81000, Vietnam

³ University of Sciences, Hue University, Hue 49000, Vietnam

bandgap energy, delaying electron–hole recombination, and enhancing the amount of catalytic and adsorptive sites.

Recently, various studies have reported that the composites prepared from ZnO and the activated carbon derived from biomass, such as brick grain particles [4], crofton weed [6], jute fibers [14], Algerian olive waste [15], wheat gluten [16], and castor leaf [17], could efficiently and stably catalyze the photodegradation of organic toxic compounds in aqueous solutions.

Longan is a subtropical fruit tree, which distributes in Asia, extending from Myanmar to southern China, southwest India and Sri Lanka, Thailand, Vietnam, etc. The world production of longan reached more than 2500 million tons in 2010, in which China, contributed about 1300 million tons, Vietnam over 600 million tons, and Thailand over 500 million tons [18]. Longan seeds account for about 17% of the total fresh fruit weight and are often discarded or burned as waste with hundreds of tons a year due to non-comprehensive use. Longan seeds, with a high content of C, O, and H, are suitable raw materials for producing activated carbon thanks to its availability [19]. Therefore, the use of this agricultural by-product as a precursor for the preparation of activated carbon not only contributes to the preparation of catalysts or adsorbents to remove organic contaminants in water but also leads to reducing the pollution caused by this source of waste products.

In the present work, the fabrication of the ZnO supported on longan-seed activated carbon (ZnO/LSAC) was performed via the carbonization of the mixture of longan seeds and zinc acetate in an alkaline medium. Methylene blue (MB) as a model dye was employed to estimate the photocatalytic activity of ZnO/LSAC. The purpose of the study is to evaluate the photocatalytic potential of ZnO/LSAC in the treatment of wastewater.

2 Experimental

2.1 Materials

The longan seeds used as a raw material to synthesize ZnO/LSAC composites in this work were obtained from Dong Thap province—Vietnam. They were pulverized to a powder of 1–2 mm, washed, and dried before use. The dried biomass samples were analyzed for ash [20], volatile matter content [21], and fixed carbon [22] (Table 1).

Zinc acetate dihydrate ($(\text{CH}_3\text{-COO})_2\text{Zn}\cdot 2\text{H}_2\text{O}$, $\geq 99.5\%$), sodium hydroxide (NaOH , $\geq 99\%$), hydrochloric acid (HCl , 37%), potassium iodide (KI , $\geq 99.5\%$), sodium chloride (NaCl , $\geq 99.5\%$), and isopropanol ($\text{CH}_3\text{CH}(\text{OH})\text{CH}_3$, $\geq 99.8\%$) were purchased from Merck. Methylene blue ($\text{C}_{16}\text{H}_{18}\text{N}_3\text{SCl}\cdot x\text{H}_2\text{O}$, 99.5%, MB), 1,4-benzoquinone ($\text{C}_6\text{H}_4\text{O}_2$, $\geq 99\%$, BQ), and dimethyl sulfoxide ($(\text{CH}_3)_2\text{SO}$,

Table 1 The content of dried longan seed

Material	Proximate analysis (dry basis) (wt %)		
	Fixed carbon	Volatile matters	Ash
Longan seed	19.18	78.93	1.88

99.9%, DMSO) were obtained from Sigma–Aldrich. All chemicals are of analytical grade and were used as received without any further purification.

2.2 Preparation of ZnO/LSAC

A required quantity of zinc acetate (5 g) and longan seed powder (10 g) were mixed in 50 mL of distilled water and stirred for 20 min at ambient temperature, then 50 mL of 1 M NaOH was added dropwise into the mixture under stirring for 180 min. The resulting solid was centrifuged and washed with water several times to completely remove the remaining NaOH and dried at 110 °C for 24 h. The final solid was carbonized in an electric furnace at 800 °C under a nitrogen atmosphere for 2 h to obtain ZnO/LSAC. The pristine ZnO was also synthesized similarly but without longan seed powder for the sake of comparison. In addition, the ZnO was also calcined at 600 °C (ZnO-600), 700 °C (ZnO-700), and 800 °C (ZnO-800) for 2 h to obtain the ZnO with different particle size.

2.3 Characterization of Materials

X-ray diffraction (XRD) was obtained on a MiniFlex 600 diffractometer (Rigaku, Japan) with the radiation source, $\text{CuK}\alpha$, $\lambda = 0.1541$ nm. The transmission electron microscopy (TEM) and high-resolution transmission electron microscopy (HRTEM) images were collected by using a JEOL JEM-2100 (USA). The particle size was calculated from TEM observation by using ImageJ and the Origin 6.0 software. The elemental composition was determined from electron dispersive X-ray (EDX) analysis coupled with HRTEM on JEOL 2100, EDX detector with XMax 80 T (Oxford). FT-Infrared (FT-IR) spectra were recorded on an IR Affinity-1S spectrophotometer (Shimadzu). DRS-UV-Vis spectra were recorded with the UV-2600 (Shimadzu) instrument, and reflectance spectra were referenced to BaSO_4 . The specific surface area (BET) was determined from the N_2 adsorption–desorption isotherms measured at liquid nitrogen temperature (77 K) on the Quantachrome TriStar 3000 V6.07A adsorption instrument. The photoluminescence spectra (PL) were measured on the Horiba Fluorolog 3 FL3-22 device with the excitation light at 365 nm.

2.4 Determination of Point of Zero Charge (pHPZC)

The point of zero charge (pH_{PZC}) of ZnO/LSAC was estimated with the pH drift method [4, 23]. Briefly, 5 mL of 0.1 M NaCl solution and 40 mL of distilled water were added to a series of 100 mL flasks. The initial pH value (pH_i) of the solution was adjusted to 2–12 by using either a 0.1 M NaOH or 0.1 M HCl solution. The total volume of solution in each flask was set exactly to 50 mL by adding distilled water. The 0.01 M NaCl solutions with different pH values were obtained. Then, 0.1 g of ZnO/LSAC was added to each flask, and the mixtures were kept on a shaker working at 180 rpm for 24 h. The final pH (pH_f) of the solutions was recorded. The difference between the initial and final pH ($\Delta pH = pH_i - pH_f$) was plotted against pH_i . The point of intersection of the curve with the abscissa, at which $\Delta pH = 0$, provides pH_{PZC} .

2.5 Photocatalytic Activity

A beaker containing 200 mL of an aqueous suspension of MB (20–70 ppm) and 50 mg of catalyst was placed under a lamp supporter. The light source is a 45 W, 220 V Compact lamp (Vietnam) equipped with a wavelength cut-off filter ($\lambda \leq 420$ nm, $d = 77$ mm). Prior to illumination, the suspension was stirred magnetically in the dark for 120 min to ensure adsorption equilibrium. Three millilitres of the suspension was withdrawn at intervals and centrifuged to remove the solid catalyst. The concentration of MB in the supernatant solution was analyzed with a UV–Vis spectrophotometer at $\lambda_{max} = 664$ nm. The degradation efficiency of MB was calculated according to Eq. (1)

$$F(\%) = 100 \times (C_0 - C) / C_0 \quad (1)$$

where C_0 and C are the concentration of the initial and remaining MB, respectively.

In the radical scavenging test, potassium iodide, benzoquinone, dimethyl sulfoxide, and isopropanol were used as scavengers. A suspension of 200 mL of MB (30 ppm) and 50 mg of catalyst was first stirred for 120 min in the dark, and then 20 mL of 2.4×10^{-2} M each radical scavenger solution was added to the mixture just after the illumination started. The MB concentration of the supernatant was determined with the spectrophotometric method, as mentioned above. The concentration of rhodamine-B, congo red, and methyl orange in solutions was also determined with the spectrophotometric method at a maximum wavelength of 552, 500, and 464 nm, respectively.

3 Results and Discussion

3.1 Characterization of Materials

Figure 1a shows the XRD patterns of ZnO calcined at 600, 700, and 800 °C. The diffraction peaks of hexagonal wurtzite ZnO are indexed as (100), (002), (101), (102), (110), (103), (200), (112), and (201) according to JCPDS-01-075-9743.

The intensity of the diffraction peaks increases with increasing calcination temperature, indicating that the higher the calcination temperature is, the higher crystallinity the material has. The crystallite size calculated according to the Scherrer equation using the (101) diffraction is around 31.23, 39.72, and 74.43 nm for the ZnO calcined at 600, 700, and 800 °C, respectively. The morphology of the ZnO calcined at 600 °C shows strong agglomerates of irregular shapes (Fig. 1b). However, the facet of the particles becomes smooth, and the particles become more even due to Ostwald's effect when the calcination temperature is higher than 700 °C (Fig. 1c, d). The particle average size of the ZnO particles calcined at 600, 700, and 800 °C is 26.37 ± 0.80 , 43.83 ± 4.09 , and 90.00 ± 16.03 nm, respectively.

The ZnO/LSAC materials with different mass ratios of $Zn(Ac)_2 \cdot 2H_2O$ and LSAC calcined at 800 °C for 2 h were synthesized (see Table S1 and Figures S1, S2) in order to estimate on the effect of the level of doping on photocatalytic activity. It was found that the ZnO/LSAC-5 (denoted as ZnO/LSAC) exhibits the highest visible-light driven photocatalytic activity. Therefore it was chosen for further experiments. Figure 2 presents the XRD patterns of LSAC and ZnO/LSAC. In Fig. 2a, the XRD pattern of LSAC exhibits the weak and broaden peaks centered at the diffraction angle of 23.7 and 44.3°, and indexed as (002) and (100) (the inset of Fig. 2a), which is characteristic of activated carbon [24, 25]. The XRD pattern of ZnO/LSAC displays the characteristic diffractions of ZnO with a lower intensity, and the peaks are broader and shifted to lower 2θ compared with the pristine ZnO (Fig. 2b), suggesting the distortion of the crystal lattice, probably due to the formation of a new bond instead of Zn–O, as reported by Yu et al. and Liu et al. [26, 27]. This result is supported by the theoretical calculation proposed by Sakong et al. [28] in which carbon atoms substitute zinc atoms in the lattice, causing the displacement of the neighboring atom and changing the lattice parameters.

The crystallite sizes of the pristine ZnO and ZnO/LSAC calcined at the same temperature (800 °C) calculated according to the Scherrer equation from the (101) diffraction are around 77.42 and 31.13 nm, respectively. The decrease of the crystallite size of ZnO in ZnO/LSAC

Fig. 1 **a** XRD patterns of ZnO calcined at different temperatures; TEM observations of ZnO calcined at **b** 600 °C; **c** 700 °C, and **d** 800 °C

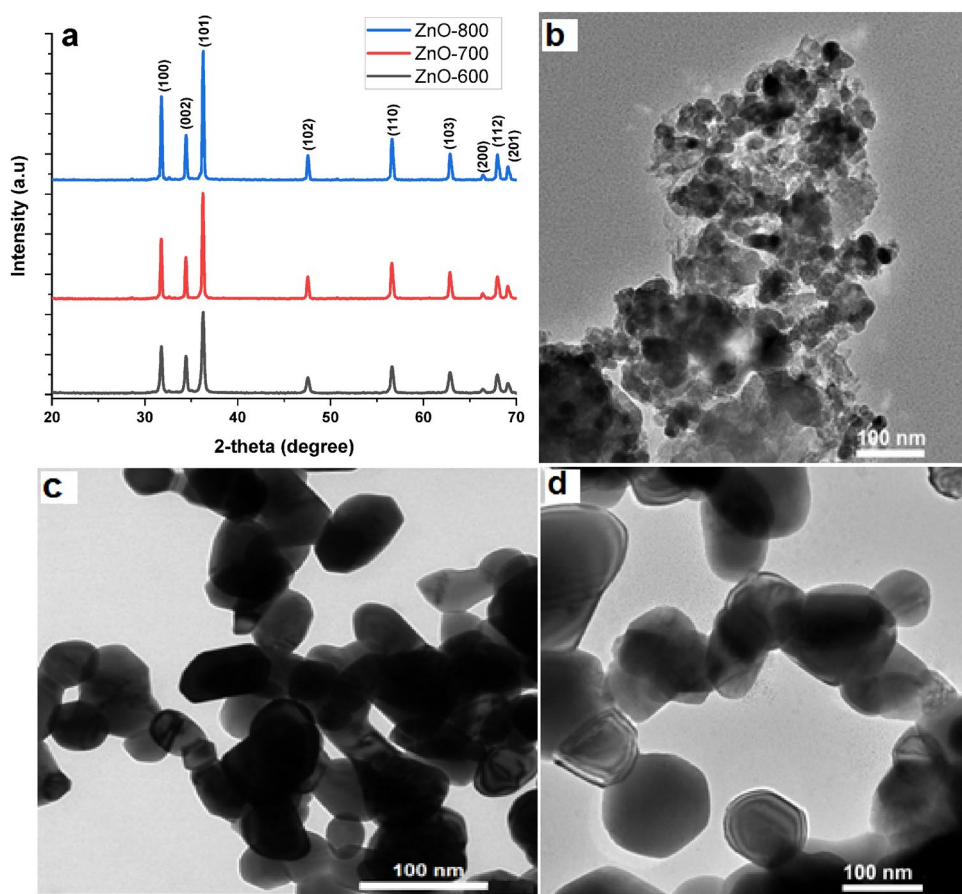
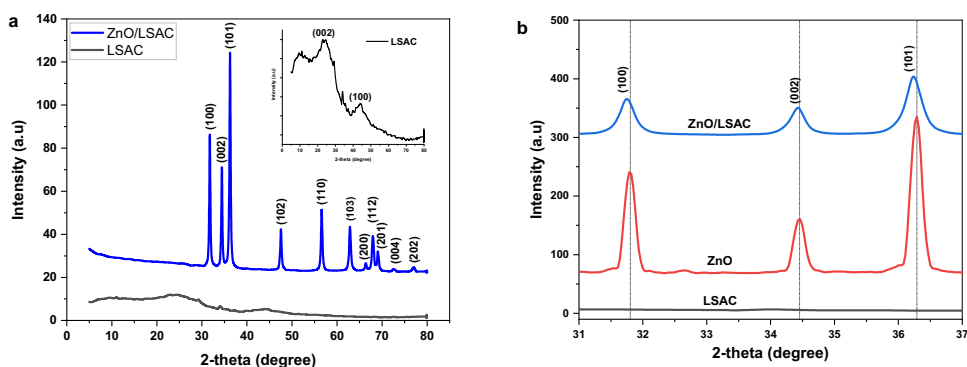


Fig. 2 **a** XRD patterns of activated carbon prepared from longan seed (LSAC) and ZnO/LSAC composite; **b** XRD patterns of pristine ZnO and ZnO/LSAC samples



is probably because the growth of ZnO crystals in the LSAC matrix is suppressed. In addition, the crystallite size of ZnO (31.13 nm) in ZnO/LSAC is similar to that of ZnO (31.23 nm) calcined at lower temperature (600 °C).

The presence of different functional groups in the synthesized ZnO/LSAC is evidenced in the FT-IR spectra (Fig. 3). In the three samples, the absorption bands in the range of 3000–3600 cm^{-1} are assigned to the stretching vibration of O–H in water [4, 29]. The absorption band with the peak centered at 2360 cm^{-1} is attributed to the CO_2 adsorbed on the sample surface [30]. On the FT-IR spectrum of AC,

the peak at 1462 cm^{-1} corresponds to C=C bond [5, 31], those at 1385 cm^{-1} and 848 cm^{-1} belong to the vibration of C–OH and COO– [4, 24, 29, 32], and those at 1106 cm^{-1} and 596 cm^{-1} are attributed to the vibration in C–H, C–C, and O–H bonds [29, 33]. On the FT-IR spectra of ZnO, a sharp peak at 448 cm^{-1} is observed as the result of Zn–O stretching vibration [4, 5, 24]. For ZnO/LSAC, the FT-IR spectrum presents the embroilment of vibrations of LSAC and ZnO, indicating the formation of ZnO/LSAC composite.

The morphologies of the obtained materials are shown on the TEM images (Fig. 4). It can be seen that the LSAC

Fig. 3 FT-IR spectra of ZnO, LSAC, and ZnO/LSAC samples

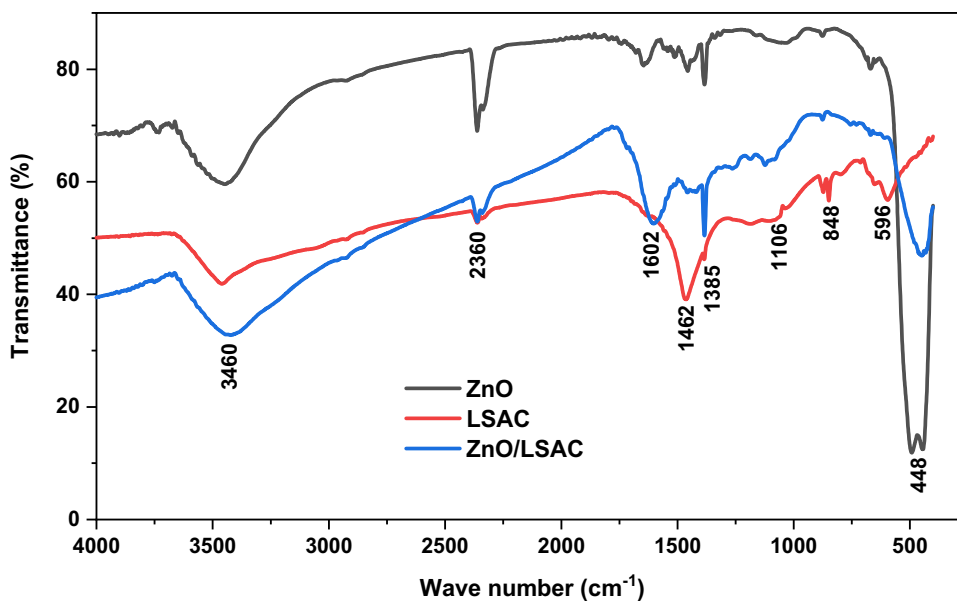
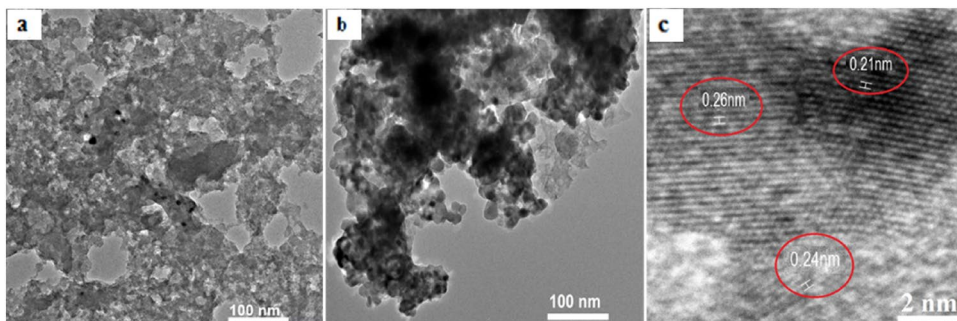


Fig. 4 TEM observations of **a** LSAC, **b** ZnO/LSAC; **c** HR-TEM observation of ZnO/LSAC



sample is composed of irregular bulk activated carbon flakes with a diameter of around several microns (Fig. 4a). For ZnO/LSAC, the ZnO particles are embedded in LSAC flakes (Fig. 4b) in which the particle size of ZnO (25.57 ± 0.49 nm) is smaller than that of the pristine ZnO (91.00 ± 16.03 nm) at the same calcination temperature but similar to that of ZnO (26.37 ± 0.80) at the calcination temperature of 600 °C (see Figure S3; Table S2,3). High-resolution images (Fig. 4c) show the lattice fringes with $d_{(002)}$ (2.6 Å) and $d_{(101)}$ (2.4 Å) spacing of wurtzite ZnO [34]. The lattice fringe with $d = 2.1$ Å corresponds to (100) planes of graphite [35].

The EDX elemental mapping observation of a selected region is presented in Fig. 5. The surface of the nanocomposite is densely covered with the ZnO particles dispersed on LSAC. The existence of Zn (Fig. 5a), O (Fig. 5b), C (Fig. 5c), and the merged picture of Zn, O, Zn, and Cu (Fig. 5d) on ZnO/LSAC confirms the spatial distributions of the elements in the structure of ZnO/LSAC. The EDX analysis further indicates the presence of C, O, and Zn components in ZnO/LSAC (Fig. 5e). The surface elemental composition is as follows: Zn 31.1%, C 33.9%, O 10.2%, and Cu

24.8%. The presence of Cu is because the measurement was conducted in a copper disk. These results evidence that the nanoparticles of ZnO are highly dispersed on the activated carbon matrix and that the synthesized ZnO/LSAC is without impurities.

The textural properties of the obtained samples were studied from the nitrogen adsorption/desorption isotherms (Fig. 6). The isotherm curves of ZnO and LSAC belong to type I and type IV with an H3 hysteresis loop, according to the IUPAC classification. ZnO has a much smaller surface area (2.7 m² g⁻¹) than LSAC (325.5 m² g⁻¹). The ZnO/LSAC is classified as type IV with an H3 hysteresis loop, and its specific surface area is 294.5 m² g⁻¹, indicating that the introduction of ZnO in LSAC significantly increases the specific area, compared with the that of pristine ZnO.

The UV–Vis diffusive reflectance spectra (UV–Vis-DRS) of ZnO, LSAC, and ZnO/LSAC are shown in Fig. 7. ZnO in ZnO/LSAC exhibits a significant redshift of the optical bandgap absorption edge to the visible light region as well as enhances light absorption in the whole UV–Vis band (Fig. 7a). Since activated carbon is an electrically

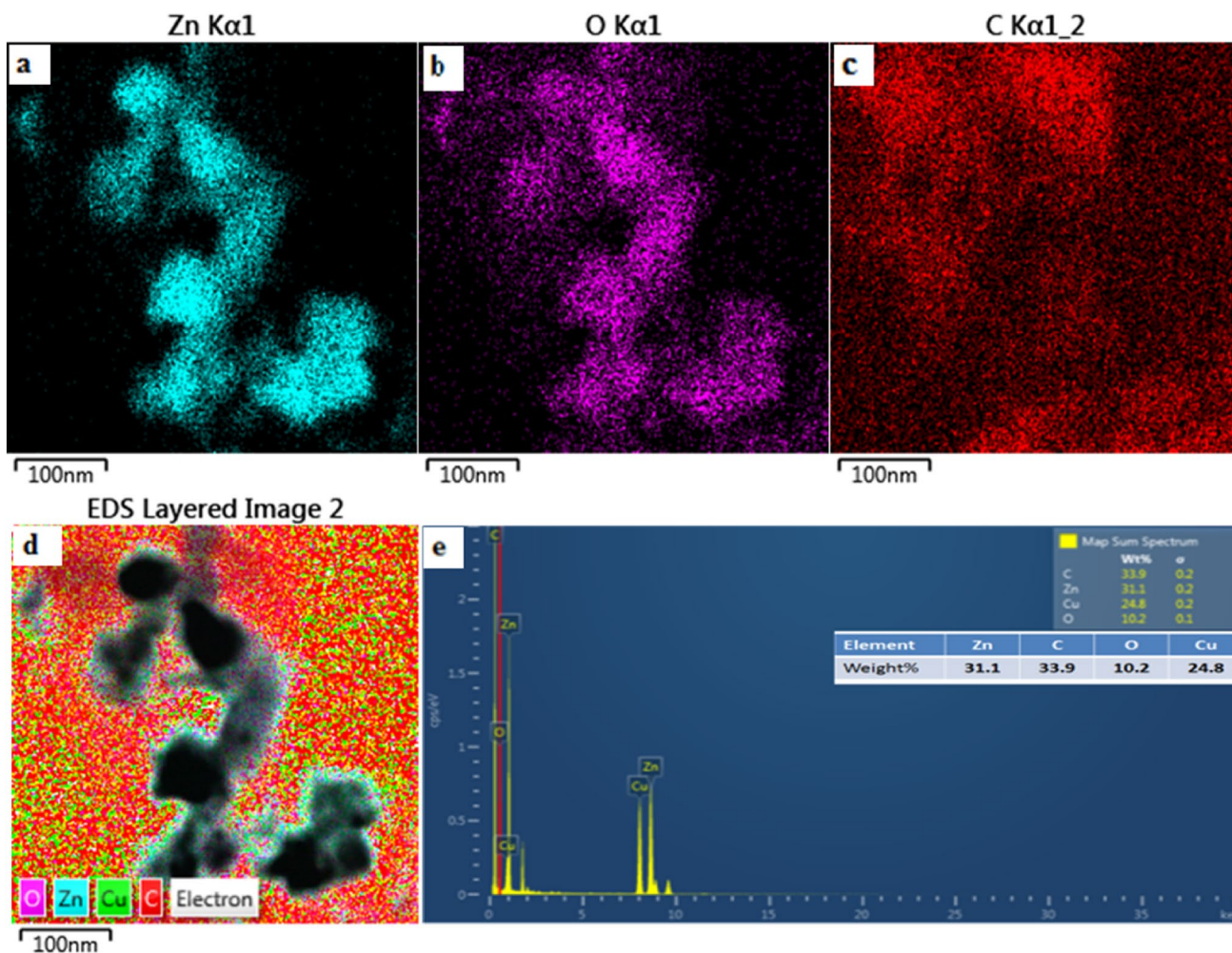


Fig. 5 EDX elemental mapping images of ZnO/LSAC: **a** Zn element; **b** O element; **c** C element and **d** the merged image of Zn, O, C and Cu elements; **e** EDX mapping spectrum of ZnO/LSAC sample

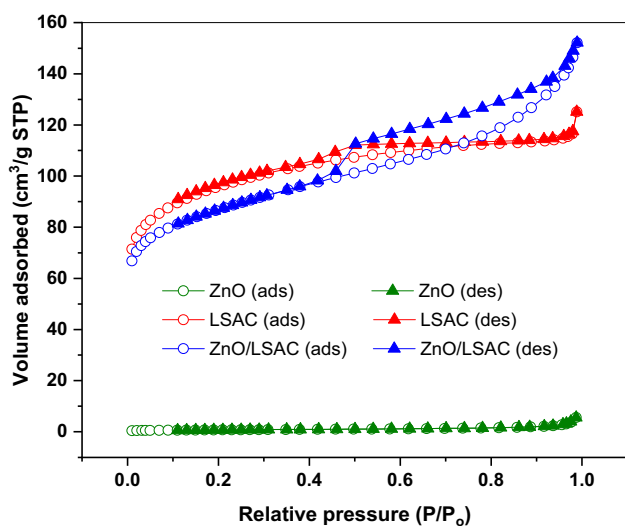


Fig. 6 Nitrogen adsorption–desorption isotherms of samples: ZnO, LSAC, and ZnO/LSAC

conductive material, its presence in ZnO/LSAC reduces the bandgap energy. The direct bandgap energies calculated from Tauc’s plot are 3.21 eV for ZnO and 2.70 eV for ZnO/LSAC (Fig. 7b).

The photoluminescence (PL) emission spectra have been widely used to study the efficiency of charge carrier trapping, immigration, and transfer in semiconductor particles. Figure 8 presents the PL spectra of the obtained samples. The PL intensity of the pristine ZnO is higher than that of ZnO/LSAC, and the reduction of PL intensity results from the decrease of the radiative recombination process. Thus, the presence of LSAC is detrimental in the e^-/h^+ recombination process under visible-light illumination. Due to the exceptional electrical conductance of activated carbon, an efficient transfer of charge carriers, and thus a longer lifetime of photogenerated electron–hole pairs are expected [36].

Fig. 7 **a** UV–Vis DRS of ZnO, ZnO/LSAC and LSAC; **b** Tauc's plots for ZnO and ZnO/LSAC

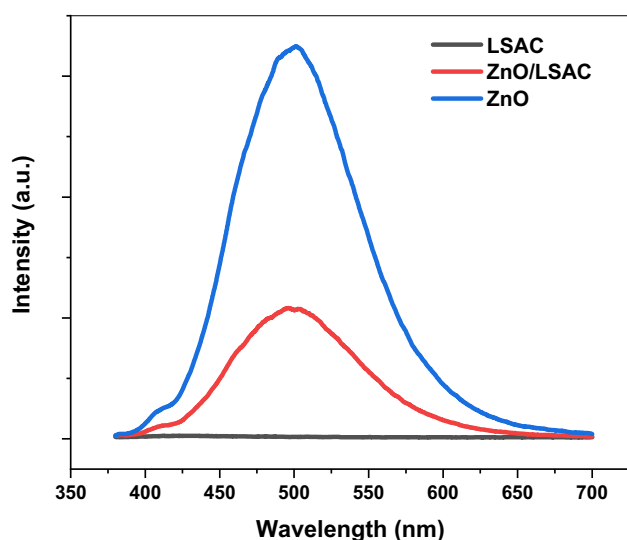
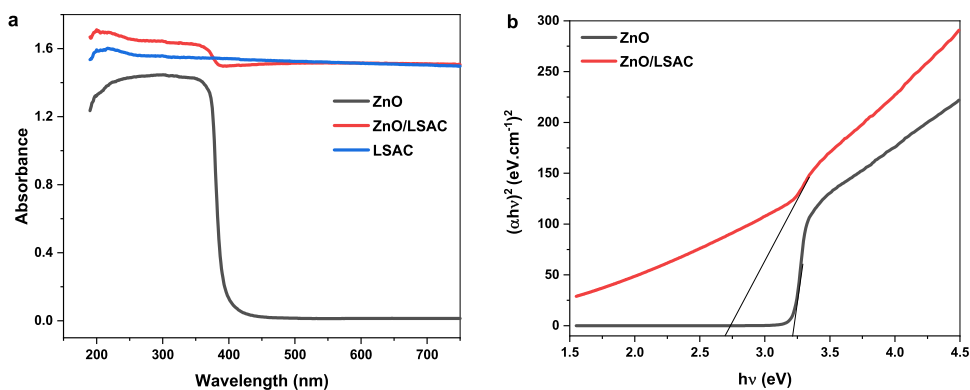


Fig. 8 Photoluminescence spectra of LSAC, ZnO and ZnO/LSAC

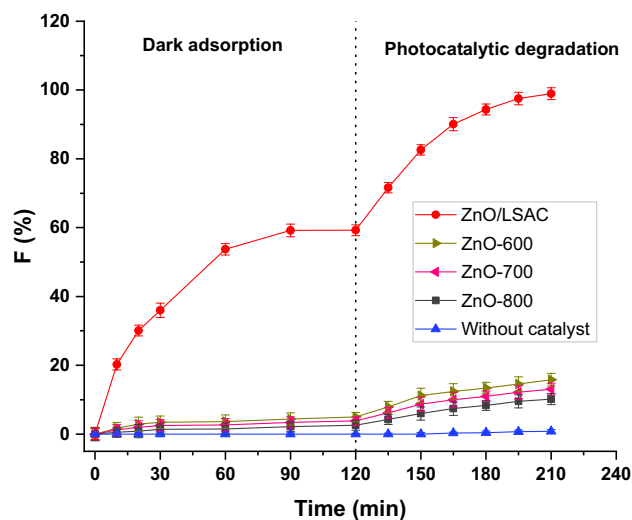


Fig. 9 Decolorization of MB with ZnO, ZnO/LSAC or without catalyst (Conditions: $V = 200$ mL; $m_{\text{catalyst}} = 50$ mg; $C_{\text{MB}} = 30$ mg L⁻¹)

3.2 Visible Light-Driven Photocatalytic Degradation of Dyes

3.2.1 Photodegradation of MB with Different Catalysts

Figure 9 presents the decolorization kinetics of MB on the ZnO synthesized at different temperatures and the ZnO/LSAC catalyst. The MB solution without catalyst was illuminated for the sake of comparison. The process was conducted for 120 min under dark adsorption to ensure the adsorption/desorption equilibrium. Then, the lamp was turned up for the photocatalytic process. The MB solution without catalyst remains decolorized after 210 min illumination, indicating MB is stable under this condition. As can be seen in Fig. 9, ZnO exhibits a low visible-light-driven photocatalytic activity, depending on the calcination temperature. It is obvious that ZnO/LSAC has a significantly higher photocatalytic activity than pristine ZnO. The photocatalytic decolorization of MB over ZnO/LSAC is 98.9%, compared with that of pristine ZnO at around 10.2 to 15.8% for all ZnO samples

after 210 min of reaction. ZnO/LSAC also adsorbs more MB than the pristine ZnO. The MB uptake on ZnO/LSAC is around 59.3% under dark adsorption, compared with 2.5–5.0% of ZnO. Although the ZnO calcined at 600 °C has similar crystallite and particle size to ZnO/LSAC (31.23 and 26.37 ± 0.80 nm for ZnO vs. 31.13 and 25.57 ± 0.49 nm for ZnO/LSAC), it has a relatively low photocatalytic activity. This indicates the vital role of LSAC in the photocatalytic activity of ZnO in ZnO/LSAC in the visible-light region.

3.2.2 Effect of pH and Leaching Experiment

The efficiency of MB decolorization increases slightly as pH varies in the range 3–6.5, followed by a significant rise between pH 6.5 and 11 (Fig. 10a). The point of zero charge (PZC) determined with the pH drift method is 6.7 (Fig. 10b), which is consistent with those of ZnO-based activated carbon [4, 15, 31, 37]. This increasing efficiency might be because of

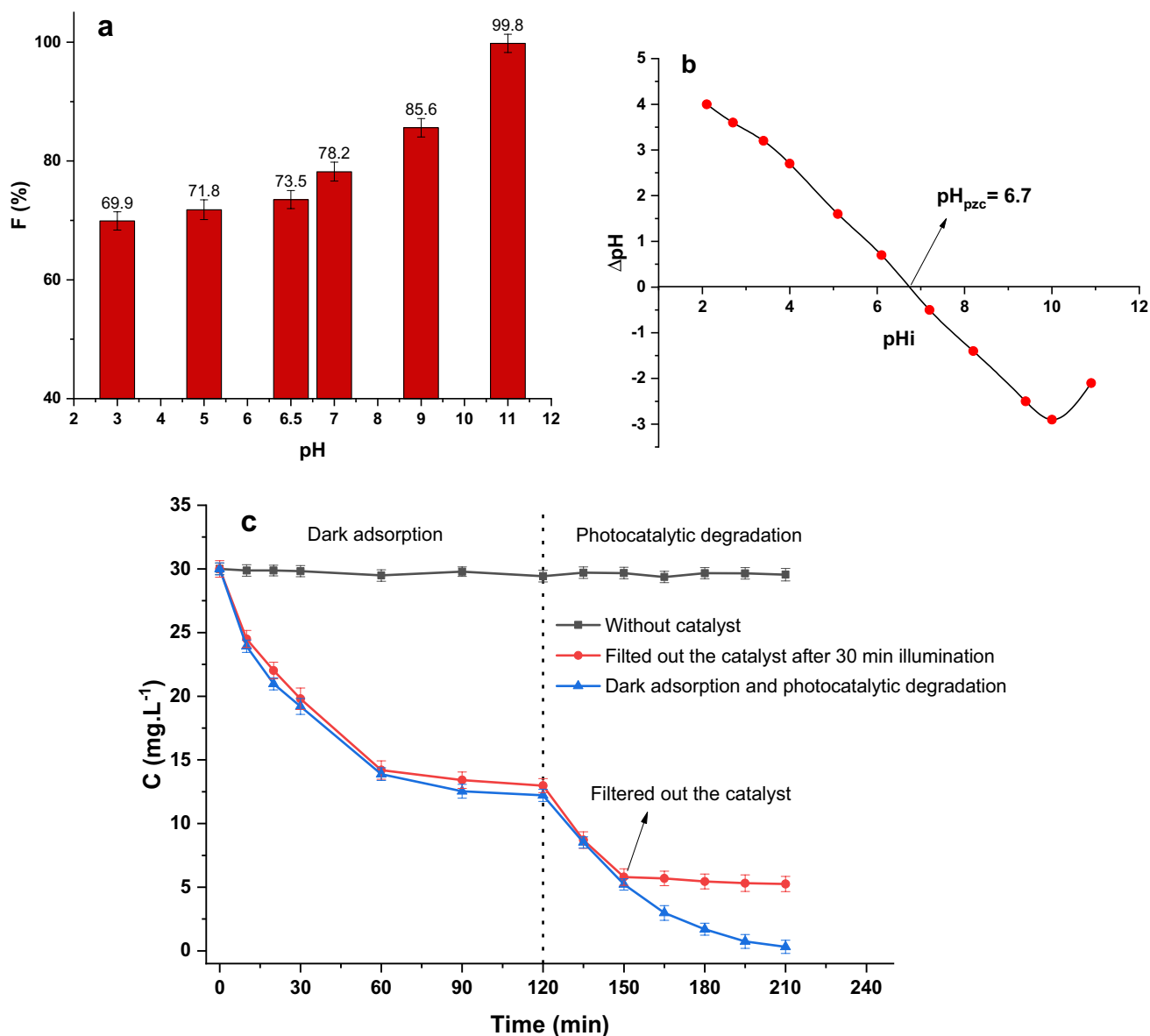


Fig. 10 **a** Effect of pH on decolorization of MB over ZnO/LSAC catalyst ($V=200$ mL, $C_0=50$ mg L⁻¹; $m_{catalyst}=50$ mg; adsorption time=120 min; illumination time=90 min); **b** the point of zero

charge obtained from the pH drift method; **c** leaching experiment ($C_0=30$ mg L⁻¹, other conditions as in **a**)

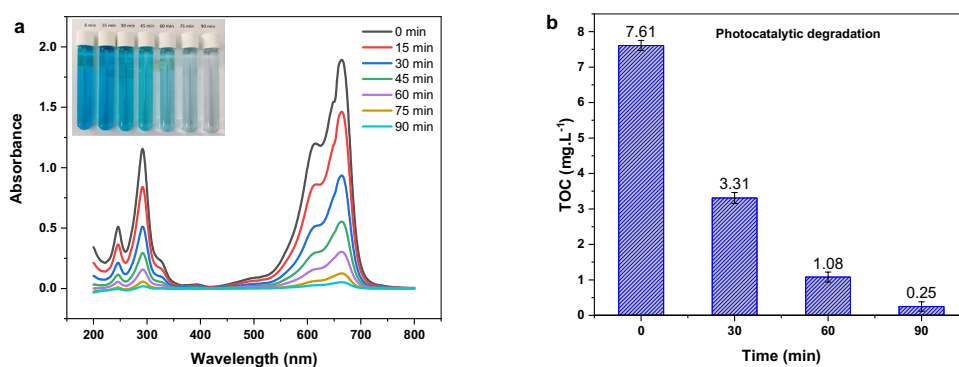
the interaction of a more negatively charged surface of ZnO/LSAC at high pH with positively charged species of MB.

In the leaching experiment, the catalyst was filtered out after 30 min of photocatalytic reaction, while the illumination continued (Fig. 10c). The decolorization almost stops after the catalyst is filtered out, indicating that ZnO/LSAC acts as a heterogeneous photocatalyst in nature.

3.2.3 Visible-Light-Driven Photocatalytic Degradation of MB

On the UV–Vis spectra of MB solution, two main absorption peaks appear at 292 and 664 nm (Fig. 11a), which are assigned to the $\pi \rightarrow \pi^*$ electron transfer in benzene rings and $n \rightarrow \pi^*$ in $-N=N-$ groups. The intensity of the

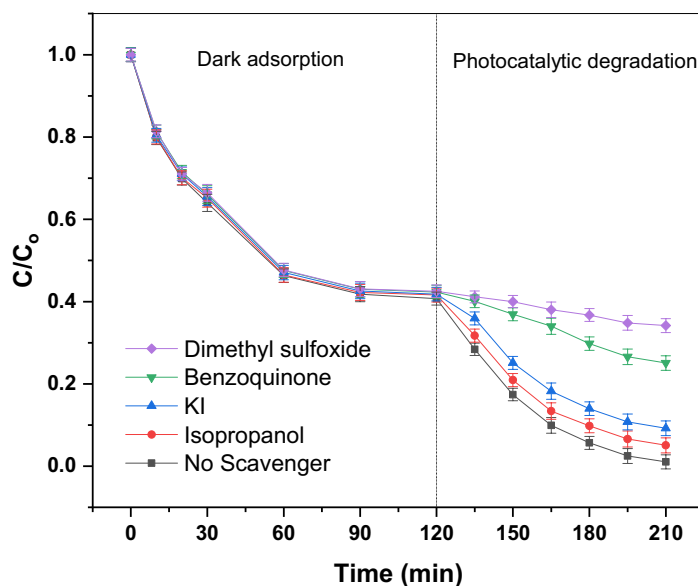
Fig. 11 **a** UV–Vis absorption spectra at different times and **b** TOC of MB solution in the photocatalytic degradation ($V=200$ mL; $C_0=30$ mg L $^{-1}$; $m_{\text{catalyst}}=50$ mg; adsorption time = 120 min; illumination time = 90 min)



absorption band decreases gradually with illumination time, and adsorption signals almost disappear after 90 min illumination. The blue color of the solution fades gradually and disappears at the end of the process. The color fade was tested by measuring TOC (Fig. 11b). The TOC value decreases from 7.61 to 0.25 mg L $^{-1}$ after 90 min of illumination.

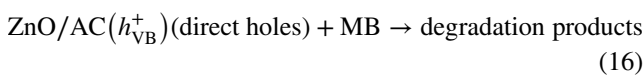
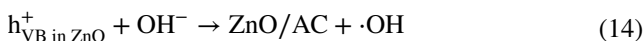
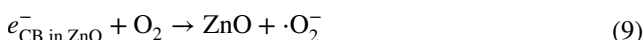
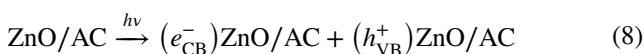
Generally, it is well-known that photodegradation is related to the oxidation of organic molecules by free radicals (hydroxyl radicals ($\cdot\text{OH}$), superoxide radicals ($\cdot\text{O}_2^-$), photo-excited holes (h^+), and excited electrons (e^-)). To study the role of radicals, degradation experiments were conducted in the presence of potassium iodide, isopropanol, benzoquinone, and dimethyl sulfoxide, which are believed to have deactivation effect on the h^+ , $\cdot\text{OH}$, $\cdot\text{O}_2^-$, and e^- species, respectively [15, 38, 39]. The decolorization efficiency decreases due to dimethyl sulfoxide by 65.8%, followed by benzoquinone (56.6%), potassium iodide (19.4%), and isopropanol reduced (9.6%). This indicates that the degradation of MB predominantly occurs via radicals in the order $e^- > \cdot\text{O}_2^- > h^+ > \cdot\text{OH}$ (Fig. 12).

Fig. 12 Effect of radical scavengers (potassium iodide, isopropanol, and benzoquinone) on MB decolorization over ZnO/LSAC catalyst ($V=200$ mL; $C_0=30$ mg L $^{-1}$; $m_{\text{catalyst}}=50$ mg; adsorption time = 120 min; illumination time = 90 min)



The photocatalytic mechanisms of semiconductors could be employed to explain the photocatalytic activity of ZnO/LSAC in the visible-light region. The adsorption edge of the conduction band for ZnO/activated carbon (E_{CB}) is -0.36 eV vs. NHE [38]; the bandgap energy (E_g) calculated from UV–Vis DRS is 2.70 eV, hence the adsorption edge of the valence band (E_{VB}) is $E_{\text{VB}} = E_{\text{CB}} + E_g = -0.36 + 2.70 = 2.34$ eV. It is known that the potential energy of HOMO and LUMO for AC is 1.85 and -0.67 eV, respectively [40], and that of MB is 1.17 eV and -0.69 eV, respectively [41, 42]. Under visible-light irradiation, activated carbon and MB act as the photosensitizers transferred their electron to the conduction band of ZnO (E_{CBZnO}) (Eqs. 2–7) [30, 40]. Because the electrons in the conduction band of ZnO is more negative (-0.36 eV) than the potential of O_2/O_2^- (-0.33 eV) [38, 43, 44], they could reduce O_2 to $\cdot\text{O}_2^-$ superoxide (Eqs. 8, 9). The superoxide radicals could react with adsorbed H_2O molecules on the surface of the catalyst or the H^+ ions present in the solution to form hydroperoxyl $\cdot\text{OH}$ radicals (Eqs. 10–13). The holes (h^+) in the valence band of ZnO/AC react with OH^- at catalyst surface to form $\cdot\text{OH}$ radicals (Eq. 14) because the holes in the valence band of ZnO/AC

(2.34 eV) are more positive than $\cdot\text{OH}/\text{OH}^-$ (1.99 eV) [43, 44]. The highly oxidizing radical ($\cdot\text{OH}$) deeply oxidizes adsorbed MB to form degraded products with a reduction in the TOC value of the dye solution (Eq. 15). In addition, the excited holes (h^+) in the VB band of ZnO/AC could react directly with MB (1.17 eV) (Eq. 16). However, the quenching experiment reveals that the oxidative pathway is negligible. From the reports [8, 15, 33, 39, 41], the possible reaction mechanism is presented as follows:



The arguments above are illustrated in Fig. 13.

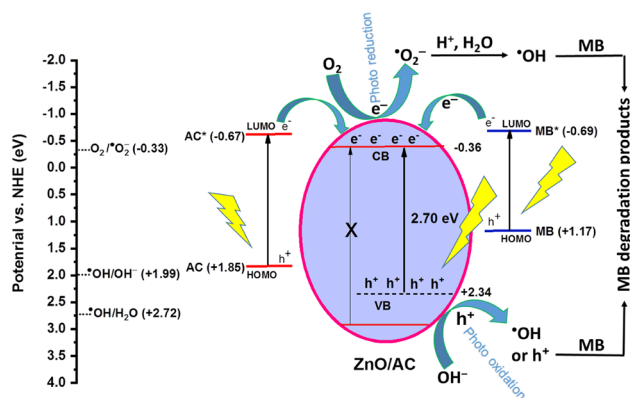


Fig. 13 Energy of valence band edge and conduction band edge for ZnO/LSAC

3.2.4 Kinetics of MB Photocatalytic Degradation

3.3 Dark Adsorption

Figure 14a presents the adsorption and photocatalytic kinetics of MB degradation. The ZnO/LSAC composite exhibits a high adsorption capacity in the dark. Depending on the initial MB concentration, the adsorption reaches adsorption/desorption equilibrium around 90–120 min. The equilibrium adsorption uptake, q_e , can be expressed as in Eq. (17) [45, 46]:

$$q_e = \frac{V \cdot (C_0 - C_e)}{m} \quad (17)$$

where C_0 and C_e are the MB concentration at initial and equilibrium time (mg L^{-1}); V is the volume of the MB solution (L); m is the mass of catalyst (g).

The relationship between C_{0e} and q_e is expressed via two isotherm models with two parameters, e.g., the Langmuir isotherm model, as in Eq. (18), and the Freundlich model, as in Eq. (19) [14, 45, 47, 48]:

$$q_e = \frac{K_L \cdot q_m \cdot C_e}{1 + K_L \cdot C_e} \quad (18)$$

$$q_e = K_F \cdot C_e^{1/n} \quad (19)$$

where q_m is the maximum monolayer adsorption uptake (mg L^{-1}); K_L is the Langmuir adsorption equilibrium constant ($\text{mg}^{-1} \text{L}$); K_F and n are Freundlich parameters.

The non-linear regressions based on the equilibrium adsorption data after 120 min of dark adsorption are shown in Table 2. Since the determination coefficient of the Langmuir isotherm model is close to 1 and higher than that of the

Fig. 14 **a** Adsorption and photodegradation kinetics of MB on ZnO/LSAC catalyst; **b** Plots of the $\frac{1}{K} \ln C + C$ against t at different initial MB concentrations

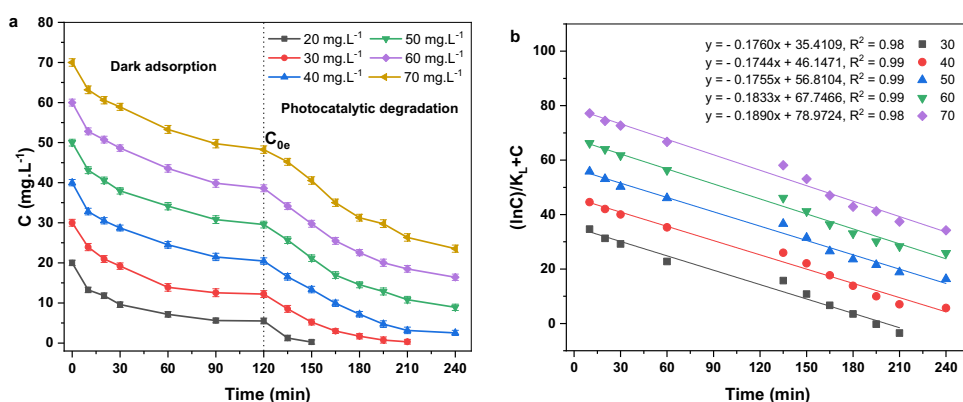


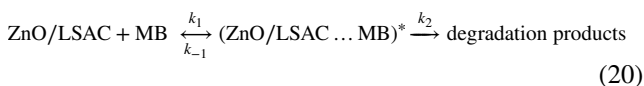
Table 2 Parameters of Langmuir and Freundlich model

Langmuir model			Freundlich model		
K_L (L mg ⁻¹)	q_m (mg g ⁻¹)	R^2	K_F	n	R^2
0.296	92.06	0.99	44.46	5.60	0.97

Freundlich isotherm model, the former fits the equilibrium data better than the latter.

3.4 Kinetics of Photocatalytic Decomposition

From the Langmuir–Hinshelwood model, the overall reaction could be illustrated as follows:



where k_1 and k_{-1} are the forward/backward adsorption rate constant, respectively; k_2 is the kinetics rate coefficient of the degradation process.

For the kinetics of unimolecular reaction on heterogeneous catalysts, the Langmuir–Hinshelwood model is widely used. This model has the following form

$$\ln \frac{C_t}{C_0} = -k_{LH} \cdot t \quad (21)$$

where k_{LH} is the rate constant of the degradation reaction (min⁻¹); C_0 and C_t are the MB initial concentration and concentration at time t (mg L⁻¹).

k_{LH} is given as the slope of the linear plot of $\ln(C_t/C_0)$ vs t .

Minh et al. [41] propose a kinetic model of the photocatalytic decomposition on heterogeneous catalyst according to the Langmuir–Hinshelwood model as follows:

$$\frac{1}{K_L} \cdot \ln C + C = -k_{MLH} \cdot t + \frac{1}{K_L} \cdot \ln C_{0e} + C_{0e} \quad (22)$$

where K_L (mg/L) is the equilibrium constant given by the Langmuir isotherm model, K_{MLH} is the rate constant of the

Table 3 The value of k_{MLH} and k_{LH} at different initial MB concentration over ZnO/LSAC

Concentration (mg L ⁻¹)	Modified Langmuir–Hinshelwood model		Langmuir–Hinshelwood model	
	K_{MLH} (mg L ⁻¹ min ⁻¹)	R^2	K_{LH} (min ⁻¹)	R^2
30	0.1760	0.98	0.0434	0.98
40	0.1744	0.99	0.0195	0.97
50	0.1755	0.99	0.0102	0.98
60	0.1833	0.99	0.0071	0.97
70	0.1890	0.98	0.0063	0.97

photocatalytic reaction, C_{0e} (mg L⁻¹) is the equilibrium concentration of adsorbate at time t (min) taken from light illumination.

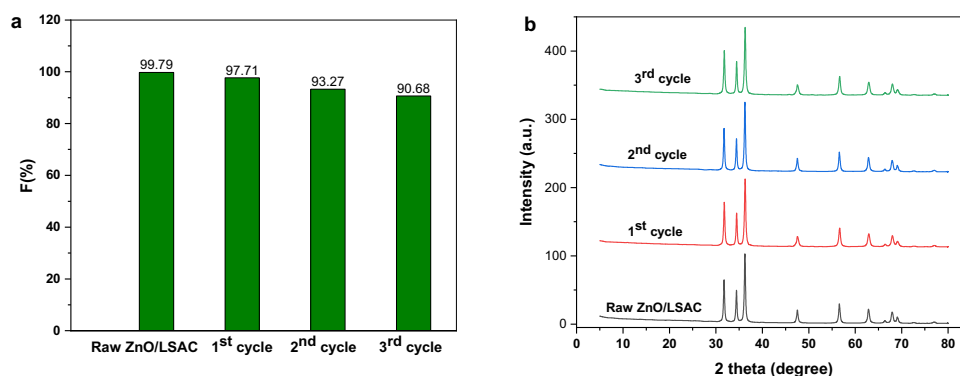
The plot of the $\left(\frac{1}{K} \ln C + C\right)$ against t gives a straight line with slope k_{MLH} (Fig. 14b). In this study, both models are applied to calculate the kinetics data for the sake of comparison, and their parameters are listed in Table 3.

The data reveal that both models have high determination coefficients ($R^2 = 0.97 \div 0.99$). However, the results of the paired samples t test show that the determination coefficients of the modified Langmuir–Hinshelwood model are significantly higher than those of Langmuir–Hinshelwood one ($t(4) = 2.27$, $p = 0.03$). This indicates that the experimental data is more compatible to the modified Langmuir–Hinshelwood model than the Langmuir–Hinshelwood model. Table 4 presents the rate constant (k_{LM}) of MB photocatalytic decomposition on various catalysts reported in the literature. It is obvious that the rate constant of the present work is compatible or higher than those in previous works, indicating that ZnO/LSAC exhibits faster kinetics.

Table 4 Comparison of rate constant of the present catalyst with those in the literature

Catalyst	S_{BET} ($m^2 g^{-1}$)	Light source	C_0 ($mg L^{-1}$)/Volume (mL)/ $m_{catalyst}$ (mg)	k_{LH} (min^{-1})	Refs.
ZnO/biochar	62.2	UV lamp light	20/100/50	0.0650	[14]
ZnO/g- C_3N_4	48	500 W metal halide lamp with a 420 nm cutoff filter	10/300/300	0.0207	[49]
ZnO/carbon nanofiber	580	13 W fluorescent lamp	10/100/100	0.0180	[50]
C-doped ZnO hybridized with g- C_3N_4	27	300 W xenon lamp with a 400 nm cutoff filter	10/100/100	0.0134	[51]
ZnO hybridized with C60	–	8 W UV lamp	3.2/100/100	0.0569	[52]
Amino-grafted GO modified ZnO	42.99	300 W Xenon lamp	10/50/10	0.0250	[53]
ZnO/rGO	101.01	UV lamp light	8.64/20/10	0.0397	[54]
N-ZnO/g- C_3N_4	–	300 W Xenon lamp	20/100//100	0.0300	[55]
ZnO/LSAC-5	294.35	45 W Compact lamp with an wavelength cut-off filter ($\lambda \leq 420$ nm)	30/200/50	0.0434	The present work

Fig. 15 **a** Photocatalytic degradation efficiency of used catalyst; **b** XRD patterns of ZnO/LSAC after three cycles of catalysis ($V=200$ mL, $C_0=30$ mg/L, $m_{catalyst}=50$ mg; adsorption time = 120 min; illumination time = 90 min)



3.4.1 Recyclability

Recycling of catalysts is one of the critical criteria to develop heterogeneous photocatalytic technology for wastewater treatment. Hence, the recyclability of ZnO/LSAC during adsorption and the photocatalytic process was performed. In this work, the used catalyst was separated, washed with ethanol several times, and dried for 24 h at 100 °C. The catalyst was used to degrade MB repeatedly and exhibits a slight loss of catalytic activity. Its efficiency remains at 90.68% after 3 cycles (Fig. 15a). The XRD patterns of the original and reused catalyst appear unchanged (Fig. 15b), indicating the stable structure of the catalyst during adsorption and photocatalysis.

In addition, the ZnO/LSAC catalyst exhibits a high catalytic activity under visible light. Figure 16 presents the photocatalytic decomposition of MB, rhodamine B, congo red, and methyl orange over pristine ZnO and ZnO/LSAC. It is notable that the photocatalytic decomposition efficiency of ZnO/LSAC is much higher than that of pristine ZnO. This leads to the conclusion that the ZnO/LSAC could catalyze

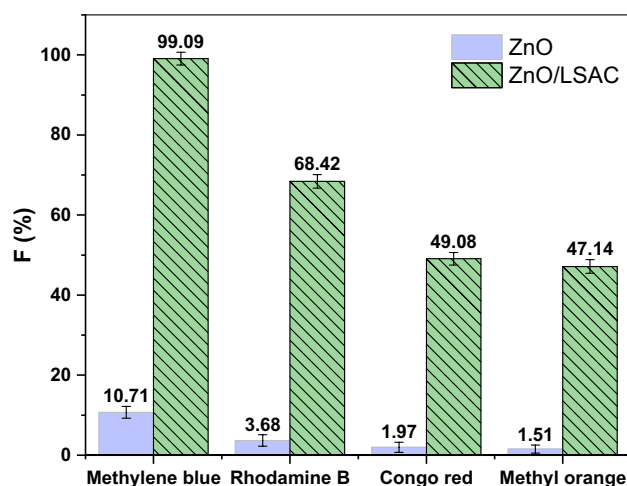


Fig. 16 Photocatalytic degradation under solar light illumination of several dyes over ZnO and ZnO/LSAC catalyst (Conditions: $C_{dyes}=30$ mg/L; $V=200$ mL; $m_{catalyst}=50$ mg; adsorption time = 120 min; illumination time = 90 min)

the dye decomposition reaction under the visible-light region.

4 Conclusion

The ZnO/activated-carbon composite was obtained via the pyrolysis of the precursor prepared from longan seeds and zinc acetate. The composite consists of nanoparticles of ZnO of around 20–30 nm in size and highly dispersed on the carbon matrix. This composite possesses a large surface and promotes visible-light absorption. The photodegradation of MB on ZnO/LSAC is 9.79 times higher than that of pristine ZnO under visible-light illumination. This enhanced photocatalytic activity is assigned to the indirect MB and activated-carbon photosensitization. The kinetics of adsorption on this material fit the modified Langmuir–Hinshelwood mode based on the combination of Langmuir isotherm and the first-order kinetic equation. The manufactured ZnO/LSAC catalyst is stable during operation. The present study proposes a good premise to obtain a less expensive photocatalyst manufactured from biomass wastes of longan seeds. This ZnO/LSAC catalyst can be effectively used for the photodegradation of various dyes from aqueous solutions.

References

- X.-Q. Qiao, Z.-W. Zhang, Q.-H. Li, D. Hou, Q. Zhang, J. Zhang, D.-S. Li, P. Feng, X. Bu, J. Mater. Chem. A **6**, 22580–22589 (2018)
- Z.-W. Zhang, Q.-H. Li, X.-Q. Qiao, D. Hou, D.-S. Li, Chin. J. Catal. **40**, 371–379 (2019)
- S.A. Khayatian, A. Kompany, N. Shahtahmassebi, A. KhorsandZak, J. Inorg. Organometall. Polym. Mater. **28**, 2677–2688 (2018)
- P. Raizada, P. Singh, A. Kumar, G. Sharma, B. Pare, S.B. Jonnalagadda, P. Thakur, Appl. Catal. A **486**, 159–169 (2014)
- M. Vinayagam, S. Ramachandran, V. Ramya, A. Sivasamy, J. Environ.Chem. Eng. **6**, 3726–3734 (2018)
- S. Cheng, Q. Chen, H. Xia, L. Zhang, J. Peng, G. Lin, X. Liao, X. Jiang, Q. Zhang, J. Clean. Product. **188**, 900–910 (2018)
- S.G. Kumar, K.S.R.K. Rao, RSC Adv. **5**, 3306–3351 (2015)
- S.V. Elangovan, V. Chandramohan, N. Sivakumar, T.S. Senthil, Superlatt. Microstruct. **85**, 901–907 (2015)
- S.N. Zailan, A. Bouaissi, N. Mahmed, M.M.A.B. Abdullah, J. Inorg. Organomet. Polym Mater. **30**, 2007–2016 (2019)
- J. Kaur, S. Singhal, Ceram. Int. **40**, 7417–7424 (2014)
- J.B. Goodall, D. Illsley, R. Lines, N.M. Makwana, J.A. Darr, ACS Comb. Sci **17**, 100–112 (2015)
- C. Shifu, Z. Wei, Z. Sujuan, L. Wei, Chem. Eng. J. **148**, 263–269 (2009)
- A.B. Patil, K.R. Patil, S.K. Pardeshi, J. Hazard. Mater. **183**, 315–323 (2010)
- M. Chen, C. Bao, D. Hu, X. Jin, Q. Huang, J. Anal. Appl. Pyrol. **139**, 319–332 (2019)
- A. Abdessemed, S. Rasalingam, S. Abdessemed, K.E.Z. Djebbar, R. Koodali, Int. J. Photoenergy **2019**, 1–13 (2019)
- M. Rezaei, S. Pirsai, S. Chavoshizadeh, J. Inorg. Organomet. Polym Mater. **30**, 2654–2665 (2019)
- B. Ulum, S. Ilyas, A.N. Fahri, I. Mutmainna, M.A. Anugrah, N. Yudasari, E.B. Demmalino, D. Tahir, J. Inorg. Organomet. Polym Mater. (2020). <https://doi.org/10.1007/s10904-10020-01631-10905>
- V.T. Pham, M. Herrero, J.I. Hormaza, Ann. Appl. Biol. **169**, 357–368 (2016)
- J. Yang, M. Yu, W. Chen, J. Ind. Eng. Chem. **21**, 414–422 (2015)
- ASTM, Standard Test Method for Total Ash content of Activate Carbon, (West Conshohocken, PA: ASTM, Philadelphia, 1996)
- ASTM, Standard Test Method for Volatile Matter Content of Activate Carbon, (West Conshohocken, PA: ASTM, Philadelphia, 1996)
- I.A.B.A. Walkley, Soil Sci. **63**, 251–263 (1934)
- O. Bechambi, S. Sayadi, W. Najjar, J. Ind. Eng. Chem. **32**, 201–210 (2015)
- J. Saini, V.K. Garg, R.K. Gupta, N. Kataria, J. Environ. Chem. Eng. **5**, 884–892 (2017)
- M. Sharma, M. Joshi, S. Nigam, S. Shree, D.K. Avasthi, R. Adellung, S.K. Srivastava, Y. Kumar Mishra, Chem. Eng. J. **358**, 540–551 (2019)
- J. Yu, T. Ma, S. Liu, Phys. Chem. Chem. Phys. **13**, 3491–3501 (2011)
- Y. Liu, H. Zhang, X. An, C. Gao, Z. Zhang, J. Zhou, M. Zhou, E. Xie, J. Alloy. Compd. **506**, 772–776 (2010)
- S. Sakong, P. Kratzer, Semiconduct. Sci. Technol. (2011). <https://doi.org/10.1088/0268-1242/1026/1081/014038>
- M. Jafari, M.R. Rahimi, M. Ghaedi, H. Javadian, A. Asfaram, J. Colloid Interface Sci. **507**, 172–189 (2017)
- M. Samadi, H.A. Shivaee, M. Zanetti, A. Pourjavadi, A. Moshfegh, J. Mol. Catal. A **359**, 42–48 (2012)
- M. Kamaraj, N.R. Srinivasan, G. Assefa, A.T. Adugna, M. Kebede, Environ Technol Innov (2020). <https://doi.org/10.1016/j.eti.2019.100540>
- Y. Li, X. Liu, Mater. Chem. Phys. **148**, 380–386 (2014)
- N. Nasseh, F.S. Arghavan, S. Rodriguez Couto, A. Hossein Panahi, M. Esmati, T.J. A-Musawi, Mater. Chem. Phys. **31**, 875–885 (2014)
- S. Cho, J.-W. Jang, J.S. Lee, K.-H. Lee, CrystEngComm **12**, 3929–3935 (2010)
- J. Mu, Z. Guo, H. Che, X. Zhang, Y. Bai, J. Hou, J. Sol-Gel. Sci. Technol. **78**, 99–109 (2015)
- Z. Chen, N. Zhang, Y.-J. Xu, CrystEngComm **15**, 3022–3030 (2013)
- G.J.F. Cruz, M.M. Gomez, J.L. Solis, J. Rimaycuna, R.L. Solis, J.F. Cruz, B. Rathnayake, R.L. Keiski, Water Sci. Technol. **2017**, 492–508 (2018)
- Y. Zhang, J. Zhou, X. Chen, Q. Feng, W. Cai, J. Alloy. Compd. **777**, 109–118 (2019)
- W. Wang, K. Xiao, L. Zhu, Y. Yin, Z. Wang, RSC Advances **7**, 21287–21297 (2017)
- X. Xu, Z. Bao, W. Tang, H. Wu, J. Pan, J. Hu, H. Zeng, Carbon **121**, 201–208 (2017)
- T.T. Minh, N.T.T. Tu, T.T. Van Thi, L.T. Hoa, H.T. Long, N.H. Phong, T.L.M. Pham, D.Q. Khieu, J. Nanomater. **2019**, 1–16 (2019)
- A.S.N. Murthy, K.S. Reddy, J. Chem. Soc. Faraday Trans. **80**, 2745–2750 (1984)
- B. Lin, C. Xue, X. Yan, G. Yang, G. Yang, B. Yang, Appl. Surf. Sci. **357**, 346–355 (2015)
- W. Wang, J.C. Yu, D. Xia, P.K. Wong, Y. Li, Environ. Sci. Technol. **47**, 8724–8732 (2013)
- S.M.A. Abdullah, F.K. Chong, J. Hazard Mater. **176**, 451–458 (2010)

46. F. Motahari, M.R. Mozdianfard, F. Soofivand, M. Salavati-Niasari, RSC Adv. **4**, 27654–27660 (2014)
47. S.M.A. Abdullah, F.K. Chong, Chem. Eng. J. **158**, 418–425 (2010)
48. X.-Q. Qiao, F.-C. Hu, F.-Y. Tian, D.-F. Hou, D.-S. Li, RSC Adv. **6**, 11631–11636 (2016)
49. X. Zhang, J. Qin, R. Hao, L. Wang, X. Shen, R. Yu, S. Limpanart, M. Ma, R. Liu, J. Phys. Chem. C **119**, 20544–20554 (2015)
50. J.H. Jeong, B.-H. Kim, Synth. Met. **247**, 163–169 (2019)
51. Y.-P. Zhu, M. Li, Y.-L. Liu, T.-Z. Ren, Z.-Y. Yuan, J. Phys. Chem. C **118**, 10963–10971 (2014)
52. H. Cheng, L. Zhang, R. Zong, Y. Zhu, J. Phys. Chem. C **113**, 2368–2374 (2009)
53. D. Zhang, Y. Zhao, L. Chen, Appl. Surf. Sci. **458**, 638–647 (2018)
54. B. Xue, Y. Zou, J. Colloid Interface Sci. **529**, 306–313 (2018)
55. Y. Liu, H. Liu, H. Zhou, T. Li, L. Zhang, Appl. Surf. Sci. **466**, 133–140 (2019)

Publisher's Note Springer Nature remains neutral with regard to jurisdictional claims in published maps and institutional affiliations.